Nano Energy 144 (2025) 111356

Contents lists available at ScienceDirect

Nano Energy

journal homepage: www.elsevier.com/locate/nanoen

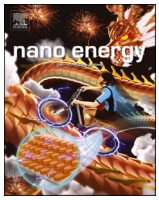

Full paper

Adaptive dual turbine triboelectric nanogenerator toward self-powered marine buoy

Yansong Gai [a], Biao Jin [a], Engui Wang [b], Yuan Bai [b], Xiaocong Jiang [a], Tianyu Sheng [a], Xiaochang Yang [a], Zhuo Liu [b,c], Yonggang Jiang [a,*], Zhou Li [b,d,**]

[a] Institute of Bionic and Micronano Systems, School of Mechanical Engineering and Automation, Beihang University, Beijing 100191, China
[b] Beijing Institute of Nanoenergy and Nanosystems, Chinese Academy of Sciences, Beijing 101400, China
[c] Ministry of Education, Beijing Advanced Innovation Center for Biomedical Engineering, School of Engineering Medicine, Beihang University, Beijing 100191, China
[d] School of Nanoscience and Engineering, University of Chinese Academy of Sciences, Beijing 100049, China

ARTICLE INFO

Keywords:
Wave energy
Self-powered marine buoy
Variable blade dual turbine
Triboelectric nanogenerator
Low crest factor

ABSTRACT

Harvesting ocean wave energy to power distributed ocean sensors has become an important research field in the construction of Marine Internet of Things (MIoTs). Triboelectric nanogenerators (TENGs) have received widespread attention in low-frequency, random, and irregular wave energy harvesting due to their excellent electromechanical conversion efficiency. However, how to efficiently convert the slow, random wave motion to drive the power generation system to generate a smooth electrical energy output is still an urgent problem to be solved. Here, a point absorber-based ocean wave energy harvesting system is designed to realize self-powered marine buoy by combining an adaptive dual-turbine wave energy converter (ADC-WEC) with a phase-shifting triboelectric nanogenerator (PS-TENG). The ADC-WEC, with variable blades, converts the up-and-down motion of the wave into a continuous unidirectional rotation that drives the PS-TENG to generate electricity. The PS-TENG converts rotational mechanical energy into direct current output with low crest factor by means of regular electrode displacements and multi-phase rectification coupling. Results show that at 600 rpm, the crest factor of the PS-TENG is down to 1.077, with a voltage of 400 V and a current of 80 μA. Importantly, the experiment showcased the buoy system harvesting wave energy to power small commercial sensors in a simulated wave environment, demonstrating its ability to build MIoTs as a self-powered marine buoy. This study presents a new solution for the efficient harvesting of wave energy and demonstrates its potential application in constructing the self-powered marine environmental monitoring networks.

1. Introduction

The Marine Internet of Things (MIoTs) serves as a pivotal enabling technology for the "blue economy," facilitating sustainable development through the seamless integration of the physical marine environment with the digital domain [1–3]. It is designed to facilitate real-time monitoring and comprehensive analysis of marine environments, resources, and associated activities by leveraging advanced intelligent sensor devices and integrated systems. Thereby enhancing the efficiency of ocean resource management, environmental protection, disaster early warning and industrial operation. With the rapid development of the MIoTs, there is an increasing demand for deploying a vast number of distributed ocean sensors, which poses a huge challenge to energy supply [4–6]. Current ocean sensors mostly use lithium batteries for power supply, and their service life is limited by battery capacity, making it difficult to achieve long-term continuous data monitoring and posing serious environmental pollution risks. To cope with the constraints of conventional power supply, it is necessary to develop sustainable and renewable in-situ energy. Wave energy exhibits high energy density, extensive spatial availability, and abundant resource potential, positioning it as an optimal renewable in-situ energy resource [7,8]. Therefore, developing efficient energy harvesting technologies to convert wave energy into electrical energy for powering ocean sensors would be a feasible energy supply strategy [9].

Triboelectric nanogenerator (TENG) based on the principles of triboelectric charging and electrostatic induction effects can effectively

* Corresponding author.
** Corresponding author at: Beijing Institute of Nanoenergy and Nanosystems, Chinese Academy of Sciences, Beijing 101400, China.
E-mail addresses: jiangyg@buaa.edu.cn (Y. Jiang), zli@binn.cas.cn (Z. Li).

https://doi.org/10.1016/j.nanoen.2025.111356
Received 15 June 2025; Received in revised form 21 July 2025; Accepted 1 August 2025
Available online 5 August 2025

convert mechanical energy into electrical energy [10–12]. Owing to its notable advantages-including low manufacturing costs, versatile operational modes, high energy conversion efficiency, and robust adaptability to low-frequency energy sources-TENG have emerged as a prominent research focus in the field of wave energy harvesting [13]. Over the past decade or so, various configurations of TENG prototype have been proposed to harvest wave energy, such as spherical shell structures [14–17], pendulum structures [18–20], cylindrical structures [21–23], bionic structures [24,25] and other different structures [26–28]. However, the above-mentioned TENG prototypes are mainly used for harvesting lateral wave energy and are susceptible to the influence of wave intensity, period, and direction, resulting in relatively low power generation efficiency. Compared with lateral waves, vertical waves have higher amplitudes and energy densities, and are insensitive to direction [29]. Therefore, there is an imperative necessity to devise novel energy conversion mechanisms capable of harvesting vertical

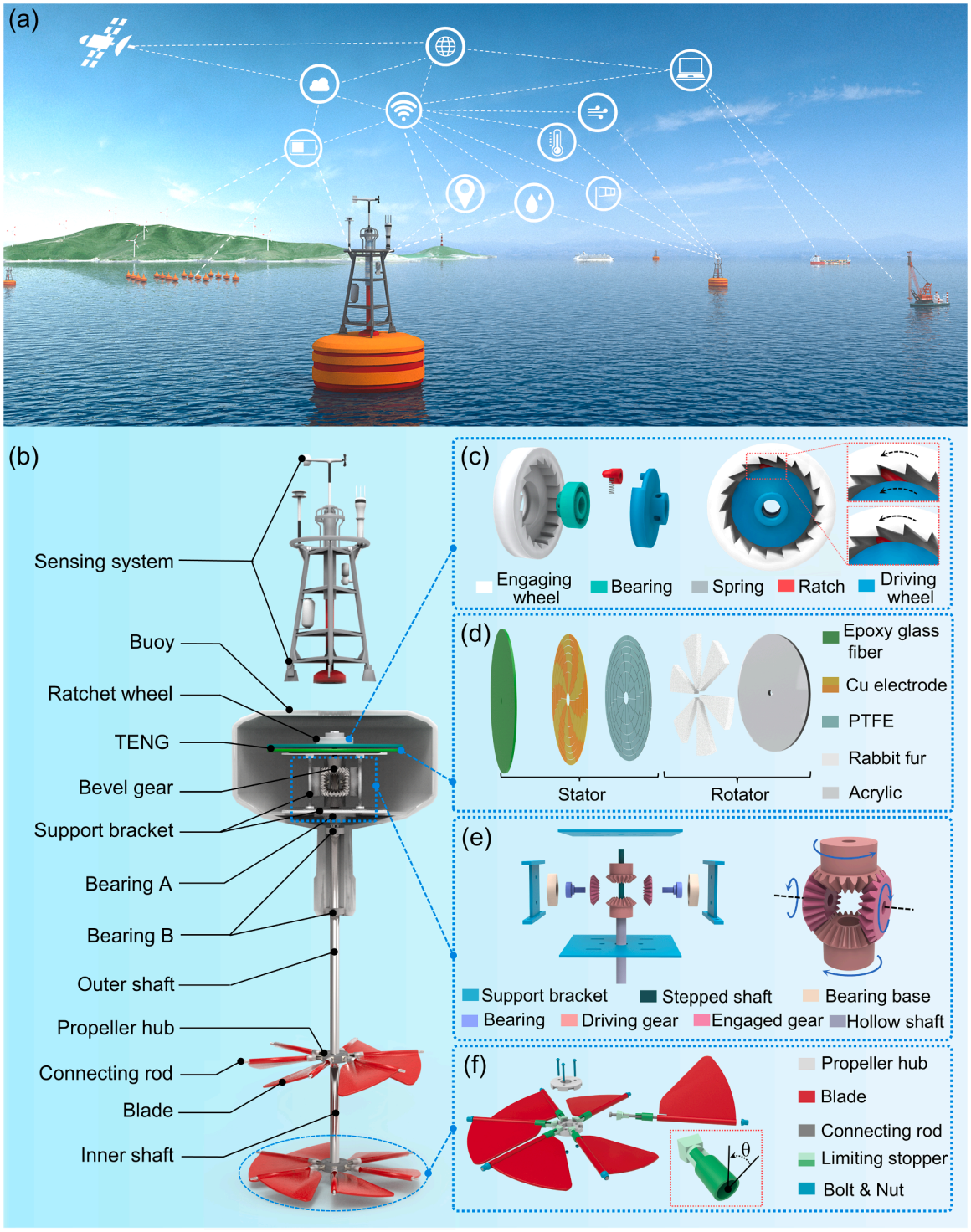

Fig. 1. Structural design of the self-powered marine buoy. **(a)** The concept of the marine monitoring system based on self-powered marine buoy. **(b)** Detailed structure of the self-powered marine buoy unit. **(c)** Structure of the one-way ratchet. **(d)** Structure of the PS-TENG. **(e)** Structure and working principle of the bevel gear transmission set. **(f)** Structure of the adaptive variable blade turbine. The inset is the enlarged view of the limiting stopper.

wave energy, thereby enhancing the overall efficiency of wave energy extraction and expanding the range of operable marine environmental conditions.

Herein, we propose a self-powered marine buoy for marine environment monitoring, which can effectively harvest vertical wave energy to power small sensors. This self-powered marine buoy is mainly composed of an adaptive dual-turbine wave energy converter (ADC-WEC) and a discoidal phase-shifted triboelectric nanogenerator (PS-TENG). The ADC-WEC converts the up-and-down motion of the wave into unidirectional rotating mechanical energy through two counter-rotating turbines, driving the PS-TENG to generate electricity. The variable blades installed on the turbine can self-adapting to the ascending and descending of wave movements, keeping the turbine rotating in one direction at all times. Meanwhile, the two turbines rotate in opposite directions, offsetting the rotational torque and making ADC-WEC more stable in water. The PS-TENG converts rotating mechanical energy into direct current (DC) electrical output with low crest factor by means of regular electrode displacement and multi-phase rectification coupling. Six radially distributed phases are designed on the stator of PS-TENG, and there is a certain angular displacement between the electrodes of different phases. When the rotor slides over each phase in sequence, the generated alternating current undergoes regular shifting, and then forms a low crest factor electrical output after rectification and coupling superposition. At 600 rpm, the crest factor of the PS-TENG is down to 1.077, with a voltage of 400 V and a current of 80 μA. Benefit from the low crest factor and excellent output performance, the PS-TENG can light up 30 bulbs with a rated power of 3 W without flickering. Importantly, in the experiments simulating ocean waves, the proposed self-powered marine buoy generated a desirable electrical output and verified its ability to power small commercial sensors. This study provides a new strategy for the efficient harvesting of wave energy and the construction of MIoTs.

2. Results and discussion

Fig. 1**(a)** illustrates the application scenarios of self-powered marine buoys in the MIoTs. These self-powered marine buoys can serve as nodes within the MIoTs, harvesting wave energy from the ocean to supply power for temperature and humidity sensing, warning lights, and small electronic components. This enables self-powered marine environmental monitoring, wireless data transmission, and related functionalities.

The design structure of the self-powered marine buoy is illustrated in Fig. 1**(b)** and **Fig. S1**. It is mainly composed of ADC-WEC, PS-TENG, buoy and sensing system. The ADC-WEC is used to convert wave energy into rotational mechanical energy, and consists of dual turbines, transmission shafts, and the gear transmission group. The upper turbine and lower turbine have the same structure, and each turbine has six fan-shaped blades, as shown in Fig. 1**(f)**. The blades can flap up and down at the preset maximum pitch angle (30°) to respond to the undulating movement of the waves. Due to the flapping movement of the blades, the upper turbine or lower turbine rotates unidirectionally along with the rise and fall of the waves. In addition, the counter-rotation of the upper and lower turbines counteracts the rotational torque, thereby enhancing the stability of the self-powered marine buoy. The rotational mechanical energy generated by the turbine was transmitted to the gear transmission set through the transmission shaft. The gear transmission set is composed of four bevel gears, with a gear meshing angle of 90°, as shown in Fig. 1**(e)**. The gear transmission system keeps the rotations of the two turbines synchronized and concentrates the mechanical energy generated by the two turbines for output. The PS-TENG was mounted on the top of the ADC-WEC. The stator of the PS-TENG was fixed on the top plate of the supporting structure of the gear transmission group, and the rotor was connected to the inner shaft by a ratchet. The design structure of the ratchet is shown in Fig. 1**(c)**, which mainly consists of engaging wheel, driving wheel and a coupled connection ratch. The engaging wheel was connected to the rotor by bolts. The driving wheel is connected to or separated from the engaging wheel by a coupled connection ratch with a spring. The hierarchical structure and photographs of PS-TENG are shown in Fig. 1**(d)** and **Fig. S2**, and it mainly composed of a stator with phase-shifted electrodes and a rotator with rabbit fur. The stator with phase-shifted electrodes was fabricated by the PCB process, and a PTFE film was covered on its surface as the negative triboelectric material. The rabbit fur, which acts as a positive triboelectric material, was cut into six sectors of the same size and shape, and then adhered to the acrylic substrate to form the rotator. The power generation system is placed inside the closed buoy, which effectively prevents the corrosion of seawater and avoid the effect of humidity on the power generation performance of the PS-TENG.

The working process of self-powered marine buoys under the wave excitation is shown in Fig. 2. The self-powered marine buoy floats on the sea surface and is able to respond to the two-stage movement of the up and down undulations of the waves. First, the buoy floats on the surface of the sea under its own buoyancy. When waves appear, the buoy rises under the thrust of the waves and pulls the underwater twin turbines through the transmission shaft. The upper surface of the turbine blades is subjected to vertical downward water flow resistance, causing the blades to deflect downward until reaching the maximum preset angle. As the buoy continues to rise, the deflected blades convert the vertical water flow resistance into rotational thrust to spin the turbine and transmission shaft. The two turbines rotate in opposite directions due to the different mounting orientations of the upper and lower turbine blades. Then, as the buoy reaches the crest of the wave, it begins to descend under its own gravity. At this point, the lower surface of the turbine blade is subjected to vertical upward water flow resistance, causing the turbine blade to deflect upwards and convert the water flow resistance into rotational thrust. Due to the self-adjusting pitch angle of the turbine blades to adapt to the direction of the water flow resistance, either the upper turbine or the lower turbine can maintain unidirectional rotation during the rising and falling stages of the wave.

During the process of the buoy fluctuating up and down with the waves, the twin turbines convert the vertical wave energy into rotational mechanical energy, which is transmitted to the bevel gear set through the transmission shaft. The bevel gear set concentrates the mechanical energy and transmits it to the rotor of the PS-TENG, driving the rotor to rotate and convert the mechanical energy into electrical energy.

The structural design and working principle of the PS-TENG are shown in Fig. 3. As shown in Fig. 3**(a)**, the stator of PS-TENG has 6 circles of electrodes distributed from the inside to the outside in a radial direction, and each circle of electrodes is a single TENG unit. We define each circle of electrodes as a phase, so that the designed PS-TENG has a total of 6 phases. Each phase has a pair of electrodes, and each pair of adjacent electrodes serves as the two electrodes of a single TENG unit. Since the triboelectric area of each phase is the same, the current or voltage output of each phase will theoretically present the same shape and amplitude. Also, due to the regular phase differences between the phases, the current or voltage of each phase undergoes a regular displacement. Therefore, coupling and superimposing the rectified current/voltage outputs for each phase results in a constant-current/voltage output, as shown in Fig. 3 **(b, c)**.

The working principle of alternating current generated by each phase of PS-TENG is represented in Fig. 3**(d)**. Since each phase is a single TENG unit, here the sixth phase is taken as an example to describe the process of generating an electron flow as the rabbit fur brush passes over the electrodes. Here, the state where the fur brush overlaps with electrode-1 is designated as the initial state (State i). Due to the different polarities of friction, the fur brushes carry positive charges, while the PTFE film carry an equal-amounts of negative charges. When the fur brush moves from electrode-1 to electrode-2, under the effect of electrostatic induction, electrons flow from electrode-1 to electrode-2 through the external load, thereby generating current (State ii). When the fur brush overlaps with electrode-2, electrons are completely transferred from electrode-1 to

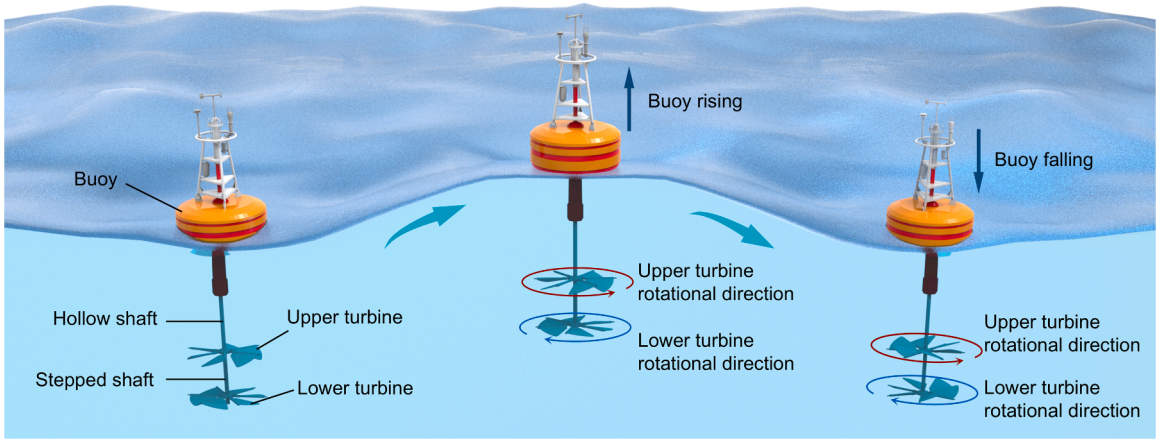

Fig. 2. Working process of the self-powered marine buoy under wave action.

electrode-2 (State iii). When the fur brush moves from electrode-2 to electrode-1, the electrons flow back from electrode-2 to electrode-1, resulting in a reverse current (State iv). Similarly, as the fur brush rotor keeps rotating, other phases will generate charge flows in sequence under the effect of phase shift. The alternating current generated in each phase undergoes rectification via an external circuit before being interconnected in parallel, ultimately producing a nearly DC output characterized by a low crest factor.

Fig. 4**(a)** shows the test device used to evaluate the output performance of the PS-TENG, in which a servo motor with adjustable speed is used to drive the PS-TENG. The triboelectric layer material affects the output performance of the TENG. Here, the influence of different triboelectric material systems on the optimization of PS-TENG is evaluated. Different pairs of triboelectric materials are labeled as stator triboelectric material @ rotor triboelectric material, namely Kapton@PTFE, Nylon@PTFE, Kapton@Rabbit Fur, Nylon@Rabbit Fur, PTFE@Rabbit Fur. As shown in Fig. 4 **(b, c)** and **Fig. S3**, at a speed of 600 rpm, the triboelectric materials pair of PTFE@Rabbit Fur has the highest output performance of the single-phase TENG. Therefore, PTFE@Rabbit Fur was chosen as the triboelectric material for the subsequent tests. Rabbit fur, as a rotor triboelectric material, forms a soft contact with the stator triboelectric material, reducing material wear and significantly improving durability.

Fig. 4**(d-f)** indicates the synchronously open-circuit voltage, short-circuit current, and transferred charge of each phase for PS-TENG at a speed of 600 rpm. It can be seen that the output characteristics of each phase maintain the same waveform, with slightly different amplitudes. The output of each phase maintains a regular phase difference, which is consistent with the previous analysis. Since the triboelectric area is the same in each phase, the output amplitude is theoretically the same in each phase. The slight difference between them is probably caused by the insufficient softness of the contact with the rabbit fur. The output performance of the single-phase TENG at different rotational speeds is shown in **Fig. S4**. The output current increases with the increase of speed, but the output voltage and transferred charge remain almost unchanged. This is because the triboelectric area of the single-phase TENG is fixed, and the triboelectric charge on the electrode surface reach saturated state at a lower speed. Fig. 4**(g)** show the output power of the single-phase TENG and PS-TENG with respect to the loading resistance at 600 rpm. The average power (P_{ave}) can be calculated by: [29,30]

$$P_{ave} = \int_0^T I(t)^2 R dt / t \tag{1}$$

where $I(t)$ is the current across the resistor at the time t, R is the load resistance, and T is the period time. It can be observed that the peak power and average power of single-phase TENG are 7 and 4.8 mW, respectively, at the matched resistance of 10^8 Ω. While the output power of PS-TENG reaches 7.56 mW at the matched resistance of 8 MΩ. The output voltages of the single-phase TENG and PS-TENG increase with the increase of the load resistance, while the output currents are the opposite (**Fig. S5**). Fig. 4 **(h)** and **(i)** show the coupling voltage and current of PS-TENG at different rotational speeds, respectively. It can be seen that the maximum value and the minimum value of the coupling current increases with the increase of rotational speed, and at the same time, the fluctuation of the amplitude also increases (Fig. 4**i** and **Fig. S6**). However, due to the fixed triboelectric area, the maximum value of the coupling voltage is basically maintained at 400 V. The minimum value and the amplitude of the coupling voltage decrease with the increase of the rotational speed (Fig. 4**h**). At 600 rpm, the PS-TENG can generate a stable DC electrical output with a voltage of 400 V and a current of 80 μA. Furthermore, the long-term stability of the PS-TENG is also explored. The values of the output current of the single-phase TENG and PS-TENG are remain stable after operate continuously at of 300 rpm for 3 h, as shown in **Fig. S7**.

To use the PS-TENG as a power source, its capacitance charging capability was tested. As shown in Fig. 5**(a)**, the smaller the capacitance, the shorter the charging time. In the continuous rotation mode of 600 rpm, the time taken by PS-TENG to charge different capacitors (470 μF, 1 mF, 2 mF, 3 mF, 4 mF and 5 mF) to 5.5 V was 28 s, 45 s, 90 s, 132 s, 202 s and 237 s, respectively. The excellent charging capacity of PS-TENG benefits from its low crest peak factor, avoiding more energy loss. The crest factor (CF) is a key indicator for evaluating the performance of direct current output, usually defined as the ratio of the maximum instantaneous current to the root-mean square. Its calculation formula are as follows: [30,31]

$$I_{rms} = \sqrt{\int_0^t I_{SC}(t)^2 dt \Big/ t} = \sqrt{\sum_{i=1}^{n} I_{sci}^2 \Big/ n} \tag{2}$$

$$CF = I_{\max} / I_{rms} \tag{3}$$

where, I_{rms} is the root-mean-square value, $I_{sc}(t)$ is the current at the time t, n is the number of the sampling points, I_{sci} is the current for the i-th sampling point, I_{max} is the maximum current. Fig. 5**(b)** illustrates the crest factors of PS-TENG at different rotational speeds. As the increase of the rotational speed, the crest factor of PS-TENG gradually reduces. At a speed of 600 rpm, the crest factor of PS-TENG is approximately constant at around 1.077, indicating good stable DC electrical generation capability. This indicates that the phase-shift design is an effective strategy to reduce the crest factor and obtain a DC output. Fig. 5**(c)** and **Table S1** show the low crest factor TENG compared with different structural designs and material selection, among which the phase-shift design

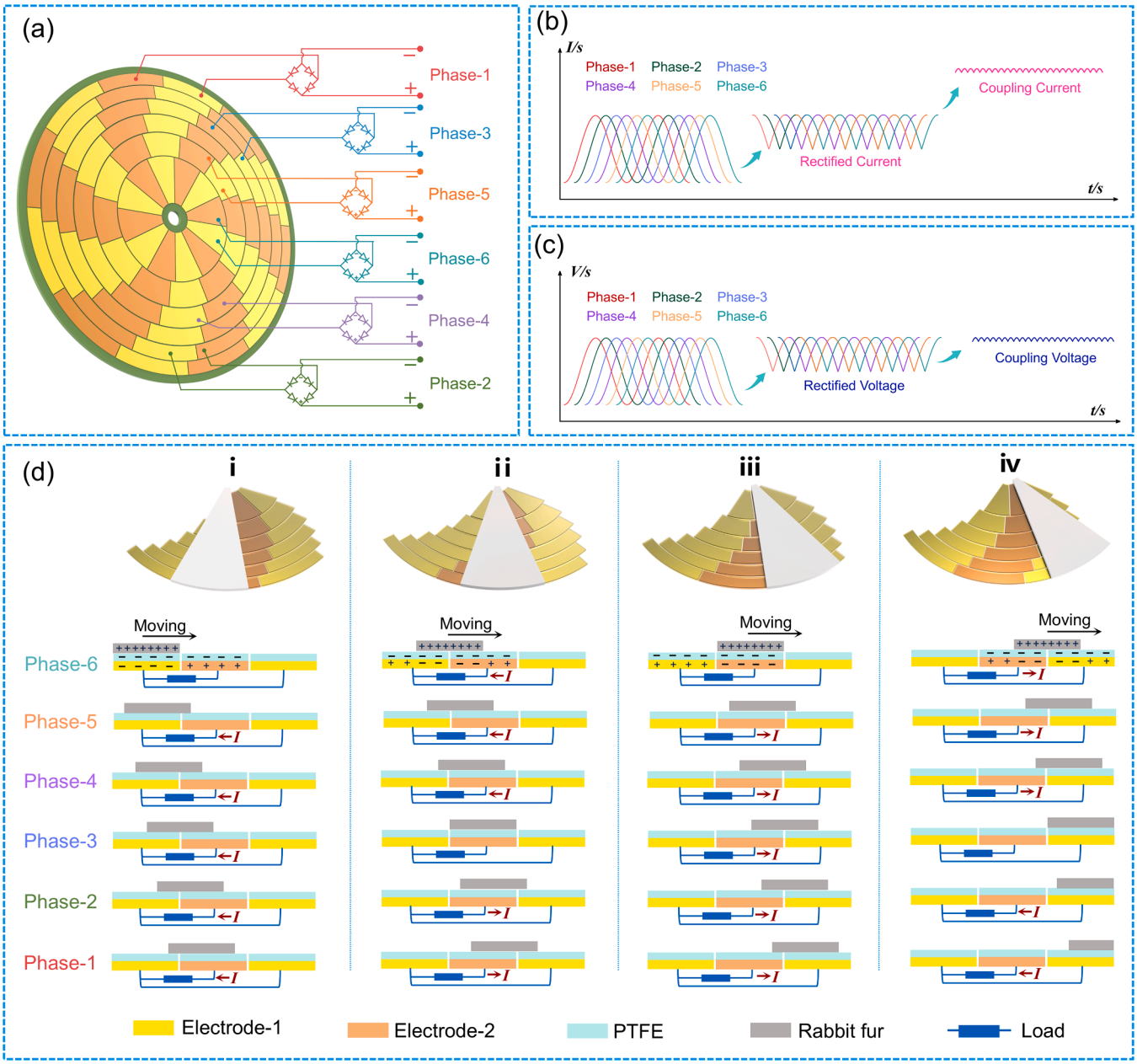

Fig. 3. Design and working principle of the PS-TENG. **(a)** Schematic circuit connection diagram of the stator for PS-TENG. **(b)** Schematic diagram of the current superposition based on the phase-shift design. **(c)** Schematic diagram of the voltage superposition based on the phase-shift design. **(d)** Working principle of the PS-TENG.

achieves a lower crest factor [32–36]. Thanks to the low crest factor, the PS-TENG can easily light up 30 commercial LED bulbs with a rated power of 3 W without any flickering, demonstrating its excellent DC output performance (Fig. 5**d** and **Movie S1**). Moreover, the PS-TENG charged a 1 mF capacitor to 3.5 V within 26 s, subsequently powering a hygro-thermograph, as shown in Fig. 5 **(e)** and **Movie S2**. Under the same conditions, the PS-TENG charged a 1 mF capacitor to 7 V within 72 s and then charge an intelligent watch, as shown in Fig. 5**(f)** and **Movie S3**. Furthermore, PS-TENG has also successfully powered the water quality analyzer, as shown in **Movie S4**. The stable DC output generated by PS-TENG can improve the charging efficiency of TENG and avoid damage to electronic components caused by pulse signals.

The adaptive dual-turbine wave energy harvesting device was driven by a linear motor to simulate its motion state during the vertical undulation of ocean waves, as shown in Fig. 6 **(a)** and **Fig. S8**. At the acceleration of 2.5 $m{\cdot}s^{-2}$, the device can output a voltage of more than 400 V and a current of 20 μA. Fig. 6**(d)** and **(e)** show the output performance of the device under different accelerations. When the acceleration gradually increases from 1 $m{\cdot}s^{-2}$ to 2.5 $m{\cdot}s^{-2}$, its output voltage increases from 300 V to 400 V and the output current increases from 7.5 μA to 20 μA. It is worth noting that in the simulation experiment, the speed of the turbine was low and constantly varied during the up and down fluctuation process (**Movie S5**), which caused the PS-TENG to be unable to operate at higher speeds, resulting in its output performance not meeting expectations. After confirming the excellent performance, the power supply capability of the adaptive variable-blade dual-turbine wave energy harvesting device for ocean related sensors toward self-powered marine environmental systems was demonstrated. As shown in Fig. 6 **(f)** and **Movie S6**, this device can effectively collect vertical wave energy to power the LED light and the hygrometer. In addition, an application system of water quality monitoring was simulated, as shown in Fig. 6 **(g, h)**. At an acceleration of 2.5 $m{\cdot}s^{-2}$, the device can charge the

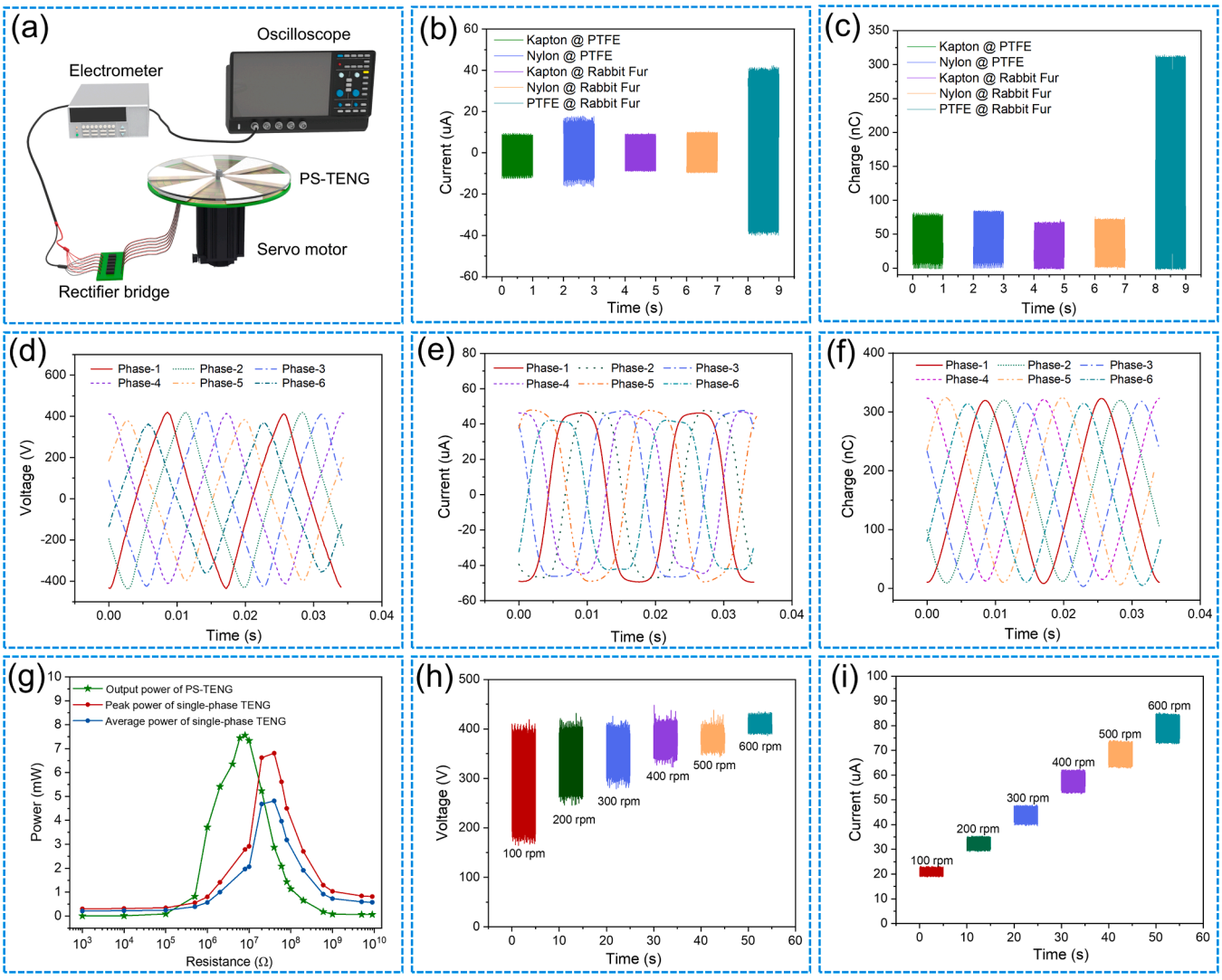

Fig. 4. Output performance of PS-TENG driven by servo motor. **(a)** Apparatus for testing the output performance of PS-TENG. **(b, c)** The short-circuit current and transferred charge of different pairs of triboelectric materials. **(d-f)** The synchronously open-circuit voltage, short-circuit current, and transferred charge for each phase of PS-TENG at 600 rpm. **(g)** Output power of single-phase TENG and PS-TENG under various loads. **(h, i)** The coupling voltage and current of PS-TENG at different rotational speeds.

5-mF capacitor to 12 V within 2730 s and successfully drive the water quality detector. The experimental results demonstrate that this self-powered marine buoy exhibits high efficiency in converting mechanical energy into electrical energy, thereby effectively powering small-scale oceanographic sensors. Furthermore, the device features a compact structural design and low manufacturing costs, presenting significant practical application advantages.

Supplementary material related to this article can be found online at doi:10.1016/j.jallcom.2022.164017.

Supplementary material related to this article can be found online at doi:10.1016/j.nanoen.2025.111356.

3. Conclusions

In summary, a marine buoy designed to capture and convert vertical wave energy for self-powered marine environment monitoring systems has been studied and demonstrated. The self-powered marine buoy system uses ADC-WEC to convert the irregular motion of wave undulations into unidirectional rotational mechanical energy, which is then used to drive the PS-TENG to rotate through a bevel gear transmission group and ratchet structure, ultimately generating electrical energy. Both the upper and lower turbines of the ADC-WEC are equipped with variable blades that can self-adapt to the ascending and descending motion of the waves, enabling the turbines to rotate unidirectionally. Furthermore, the two turbines rotate in opposite directions, offsetting the rotational torque and enhancing the stability of the ADC-WEC in water. Benefiting from regular electrode displacements and multi-phase rectification coupling, PS-TENG achieves DC output with a low crest factor. At 600 rpm, the crest factor of the PS-TENG is down to 1.077, with a voltage of 400 V and a current of 80 μA. According to wave simulation experiments, the self-powered marine buoy system can output approximately 400 V and 20 μA under the excitation conditions of an acceleration of 2.5 $m \cdot s^{-2}$. Importantly, the self-powered marine buoy system has been demonstrated to be capable of powering small sensors such as thermometers and water quality detectors, as well as enabling data acquisition functions. As it should be, this work still poses challenges in enhancing the turbine power, increasing the rotation speed of the TENG and the power management, which will be an issue that needs to be addressed in future research. In conclusion, this work provides a promising strategy for the efficient harvesting of wave energy and the construction of a self-powered marine environment monitoring network.

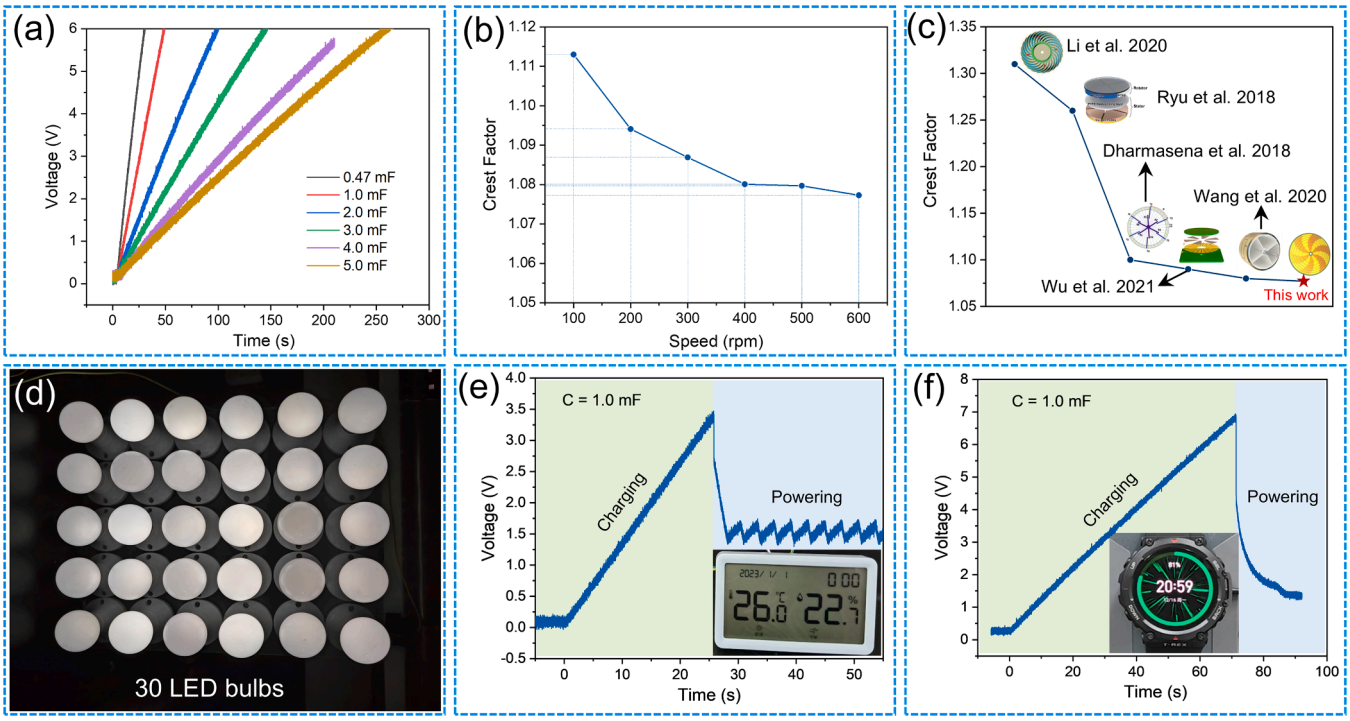

Fig. 5. **(a)** The charging performances of PS-TENG for different capacitors at 600 rpm. **(b)** The crest factor of PS-TENG at different speeds. **(c)** The crest factor of this work compared with that reported by others. **(d)** 30 LED bulbs can be lighted up directly by PS-TENG at 600 rpm. **(e)** Charging 1.0 mF capacitor to drive a hygrothermograph at 600 rpm. **(f)** Charging 1.0 mF capacitor to drive a smartwatch at 600 rpm.

4. Experimental section

4.1. Fabrication of the variable blade twin turbine energy conversion device

The twin-turbine energy conversion device was designed and modeled using Solidworks. It is mainly composed of the gear transmission group, the drive shaft, and the turbine. The gear drive group consists of 4 bevel gears (mold: 1.5, number of teeth: 20, engagement angle: 90°) and a support structure. The four plates of the support structure are made of aluminum alloy. The inner shaft of the drive shaft is a solid steel shaft with a length of 120 cm and a diameter of 8 mm. The outer shaft of the drive shaft is a hollow shaft, with a length of mostly 85 cm, an outer diameter of 14 mm, and an inner diameter of 12 mm. Both ends of the outer shaft are equipped with flange bearings. The inner diameter of the flange bearing is 8 mm, the outer diameter is 12 mm, and the flange diameter is 13.6 mm. The turbines are composed of blades, connecting rods, limiting stoppers, and propeller hubs. Its design drawing is shown in **Figure S9**. The propeller blades were 3D printed from PLA material. The connecting rods, limiting stoppers, and propeller hubs are all machined from steel. The connecting rods are used to install the blades, with a length of 126 mm and a diameter of 3.5 mm. The opening angle of the limiting stopper is 120°, which can limit the rotation angle of the blade. The rotation angle can be adjusted through a 3D printed collar, with a maximum rotation angle of 30°. The assembled variable blade turbine is about 280 mm in diameter. Two variable blade turbines are installed on the inner and outer shafts respectively through 3D printed connectors, with a spacing of 25 cm.

The PS-TENG was mounted on the top of the variable-blade twin-turbine energy conversion device. The stator of the PS-TENG was fixed on the top plate of the support structure of the gear transmission group, and the rotor was connected to the inner shaft by a one-way ratchet. The one-way ratchet was 3D printed and mainly consists of engaging wheel, driving wheel and a coupled connection ratch. The inner and outer edges of the engaging wheel were 40 mm and 56 mm respectively. The inner edge was designed with ratchet teeth, and the number of ratchet teeth is 18. The engaging wheel was connected to the rotor by bolts. The diameter of the driving wheel is 36 mm, and the center of which was drilled through hole of 8 mm to connect with the inner drive shaft. The driving wheel is connected or separated from the engaging wheel by the coupled connection ratch with spring.

4.2. Fabrication of the PS-TENG

The PS-TENG consisted of a stator with phase-shifted electrodes and a rotator with rabbit fur. The stator was fabricated by PCB technology with an inner diameter of 10 mm and an outer diameter of 105 mm, as shown in **Fig. S10(a)**. The stator has 6 radially distributed phases, and each phase has 12 copper electrodes. The thickness of the copper electrode layer is 35 m and the gap between the electrodes is 0.5 mm. Note that all electrodes have the same area. An 80-μm-thick PTFE film was adhered to the copper electrodes as a triboelectric layer. The rotator was laser-cut from a 5-millimeter-thick acrylic plate, with the same inner and outer diameters as the stator disk, as shown in **Fig. S10(b)**. The rabbit fur was cut into 6 sectors of the same size and shape, and then adhered to the acrylic circular substrate to form the rotator.

4.3. Characterizations and measurements

The rotating motion of the PS-TENG was driven by a commercial motor (57HSE2.2 N), which can provide different speeds. The performance of the PS-TENG was measured using a programmable electrometer (Keithley 6517B) and an oscilloscope (Teledyne LeCroy HDO 8108 A). A linear motor (LinMot BR01–37) was used to provide a periodic motion with different accelerations for simulating the heaving motion generated by ocean waves.

CRediT authorship contribution statement

Yansong Gai: Writing – review & editing, Writing – original draft,

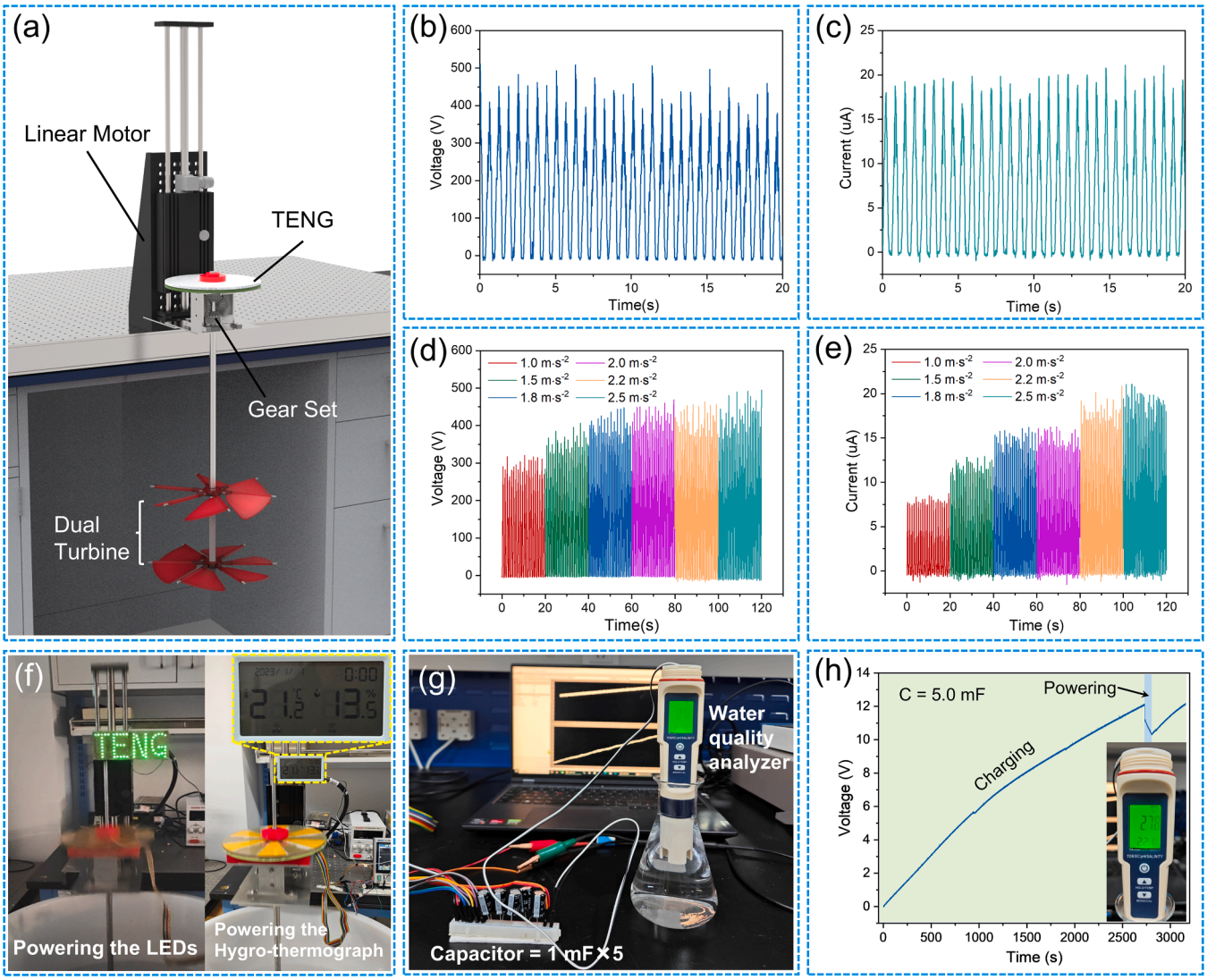

Fig. 6. Application and output performance of the adaptive variable blade dual turbine wave energy harvesting device in simulating environment. **(a)** Simulation test equipment of the adaptive variable blade dual turbine wave energy harvesting device. **(b, c)** The output voltage and current at 2.5 $m{\cdot}s^{-2}$. **(d, e)** The output voltage and current at different acceleration. **(f)** The adaptive variable blade dual turbine wave energy harvesting device powering the LEDs and hygro-thermograph. **(g)** Charging 5.0 mF capacitor to drive a water quality detector. **(h)** The voltage of capacitor of 5.0 mF when powering the water quality detector.

Methodology, Data curation, Conceptualization. **Yonggang Jiang:** Writing – review & editing, Supervision, Resources. **Zhou Li:** Writing – review & editing, Supervision, Resources. **Xiaochang Yang:** Data curation. **Zhuo Liu:** Writing – review & editing, Methodology. **Xiaocong Jiang:** Data curation. **Tianyu Sheng:** Methodology, Data curation. **Engui Wang:** Validation, Methodology, Data curation. **Yuan Bai:** Validation, Methodology, Data curation. **Biao Jin:** Validation, Methodology, Data curation.

Declaration of Competing Interest

The authors declare that they have no known competing financial interests or personal relationships that could have appeared to influence the work reported in this paper.

Acknowledgements

This study was supported by the National Natural Science Foundation of China (T2121003 to Y. Jiang; T2125003 to Z. Li), the National Key Research and Development Program of China (2023YFB3208000 to Y. Jiang; 2022YFE0111700 to Z. Li), the Postdoctoral Fellowship Program of China Postdoctoral Science Foundation (GZC20233373 to Y. Gai), the Beijing Natural Science Foundation (L244011 to Y. Gai), the Scientific and Technological Innovation Project of China Academy of Chinese Medical Sciences (CI2023C020YL to Z. Liu).

Appendix A. Supporting information

Supplementary data associated with this article can be found in the online version at doi:10.1016/j.nanoen.2025.111356.

Data Availability

Data will be made available on request.

References

[1] Y. Lou, M. Li, A. Yu, J. Zhai, Z.L. Wang, From wave energy to electricity: functional design and performance analysis of triboelectric nanogenerators, NanoMicro Lett. 17 (2025) 298.
[2] C. Shang, Y. Chen, Z. Dai, Y. Yalikun, L. Qian, P.S. Lee, Y. Yang, Nanotechnology-enabled devices for ocean Internet of things, EcoMat 7 (2025) 70003.

[3] J. He, X. Wang, Y. Nan, H. Zhou, Research progress of triboelectric nanogenerators for ocean wave energy harvesting, Small 21 (2025) 2411074.
[4] T. Bhatta, P. Maharjan, K. Shrestha, S. Lee, M. Salauddin, M.T. Rahman, S.M. S. Rana, S. Sharma, C. Park, S.H. Yoon, J.Y. Park, A hybrid self-powered arbitrary wave motion sensing system for real-time wireless marine environment monitoring application, Adv. Energy Mater. 12 (2021) 2102460.
[5] Y. Nan, X. Wang, H. Xu, H. Zhou, Y. Sun, M. Wang, W. Liu, C. Ma, T. Yu, Submerged and completely open solid-liquid triboelectric nanogenerator for water wave energy harvesting, InfoMat 7 (2024) e12621.
[6] Z. Lu, L. Zhao, H. Fu, E. Yeatman, H. Ding, L. Chen, Ocean wave energy harvesting with high energy density and self-powered monitoring system, Nat. Commun. 15 (2024) 6513.
[7] T. Li, X. Wang, K. Wang, Y. Liu, C. Li, F. Zhao, Y. Yao, T. Cheng, Bidirectional rotating turbine hybrid triboelectric-electromagnetic wave energy harvester for marine environment monitoring, Adv. Energy Mater. 14 (2024) 2400313.
[8] S. Panda, S. Hajra, Y. Oh, W. Oh, J.H.Y. Lee, H. Shin, V. Vivekananthan, Y. Yang, Y. K. Mishra, H.J. Kim, Hybrid nanogenerators for ocean energy harvesting: mechanisms, designs, and applications, Small 19 (2023) 2300847.
[9] C. Zhang, Y. Hao, J. Yang, W. Su, H. Zhang, Z.L. Wang, J. Wang, X. Li, Magnetic suspension damped hybrid nanogenerator for water wave energy harvesting, Adv. Energy Mater. 15 (2025) 2500130.
[10] D. Jiang, T. Wang, E. Wang, J. Xue, W. Diao, M. Xu, L. Luo, Y. Zhao, X. Yuan, J. Wang, L. Ruan, H. Ouyang, Z. Li, Q. Wang, Triboelectric and iontronic dual-responsive bioinspired ionic skin for human-like dexterous robotic manipulation, Nano Energy 131 (2024) 110257.
[11] Y. Gai, Y. Bai, Y. Cao, E. Wang, J. Xue, X. Qu, Z. Liu, D. Luo, Z. Li, A gyroscope nanogenerator with frequency up-conversion effect for fitness and energy harvesting, Small 18 (2022) 2108091.
[12] X. Qu, S. Cheng, Y. Liu, Y. Hu, Y. Shan, R. Luo, S. Weng, H. Li, H. Niu, M. Gu, Y. Fan, B. Shi, Z. Liu, W. Hua, Z. Li, Z.L. Wang, Bias-free cardiac monitoring capsule, Adv. Mater. 36 (2024) 2402457.
[13] S. Yang, S. Wang, L. Zhang, P. Jia, Y. Feng, Y. Guo, Y. Wang, Y. Zhang, B. Li, C. Hao, Swing-arm triboelectric nanogenerator for efficient wave energy harvesting, ACS Appl. Mater. Interfaces 17 (2025) 19054–19061.
[14] Z. Yuan, C. Wang, J. Xi, X. Han, J. Li, S. Han, W. Gao, C. Pan, Spherical triboelectric nanogenerator with dense point contacts for harvesting multidirectional water wave and vibration energy, ACS Energy Lett. 6 (2021) 2809–2816.
[15] S. Jia, X. Yang, W. Feng, L. Liu, L. Zhao, L. Wu, S. Li, W. Zuo, Q. Tang, T. Jiang, Z. L. Wang, Self-adaptive gyroscope-structured hybrid triboelectric-electromagnetic buoy system for real-time ocean currents monitoring, Small 21 (2025) 2501073.
[16] X. Liang, T. Jiang, G. Liu, T. Xiao, L. Xu, W. Li, F. Xi, C. Zhang, Z.L. Wang, Triboelectric nanogenerator networks integrated with power management module for water wave energy harvesting, Adv. Funct. Mater. 29 (2019) 1807241.
[17] W. Gao, X. Gao, J. Su, H. Cai, H. Li, B. Chen, Z.L. Wang, Gyro-multigrid triboelectric nanogenerator via topological defects strategy for efficiently harvesting low-grade wave energy, Adv. Energy Mater. (2025) 2405398.
[18] Y. Sun, F. Zheng, X. Wei, Y. Shi, R. Li, B. Wang, L. Wang, Z. Wu, Z.L. Wang, Pendular-translational hybrid nanogenerator harvesting water wave energy, ACS Appl. Mater. Interfaces 14 (2022) 15187–15194.
[19] W. Liu, X. Wang, L. Yang, Y. Wang, H. Xu, Y. Sun, Y. Nan, C. Sun, H. Zhou, Y. Huang, Swing origami-structure-based triboelectric nanogenerator for harvesting blue energy toward marine environmental applications, Adv. Sci. 11 (2024) 2401578.
[20] Y. Xu, W. Yang, X. Lu, Y. Yang, J. Li, J. Wen, T. Cheng, Z.L. Wang, Triboelectric nanogenerator for ocean wave graded energy harvesting and condition monitoring, ACS Nano 15 (2021) 16368–16375.
[21] J. Zhang, H. Li, J. Wang, S. He, X. Wang, Y. Yu, J. Zhu, X. Cheng, L. Jiang, Z. L. Wang, T. Cheng, A flexible rolling triboelectric nanogenerator with a bionic gill cover structure for low-velocity water flow energy harvesting, Small 21 (2025) 2409864.
[22] Z. Wu, B. Zhang, H. Zou, Z. Lin, G. Liu, Z.L. Wang, Multifunctional sensor based on translational-rotary triboelectric nanogenerator, Adv. Energy Mater. 9 (2019) 1901124.
[23] X. Wang, H. Li, J. Zhang, S. He, J. Wang, Y. Zhao, X. Guo, Y. Yu, Z.L. Wang, T. Cheng, Achieving dual-function in situ monitoring of water level and flow velocity via a flapping-wing triboelectric nanogenerator, Adv. Funct. Mater. (2025) 2506045.
[24] R. Lei, H. Zhai, J. Nie, W. Zhong, Y. Bai, X. Liang, L. Xu, T. Jiang, X. Chen, Z. L. Wang, Butterfly-inspired triboelectric nanogenerators with spring-assisted linkage structure for water wave energy harvesting, Adv. Mater. Technol. 4 (2019) 1800514.
[25] J. Zhang, H. Li, J. Wang, S. He, X. Wang, Y. Yu, J. Zhu, X. Cheng, L. Jiang, Z. L. Wang, T. Cheng, A flexible rolling triboelectric nanogenerator with a bionic gill cover structure for low-velocity water flow energy harvesting, Small 21 (2025) 2409864.
[26] F. Chen, X. Dai, X. Wu, Z. Ding, Y. Gao, Y. Pang, T. Jiang, J. Luo, Z. Hong, Z. L. Wang, High energy density non-contact bidirectional spinning oscillating float-type triboelectric nanogenerators for energy extraction from irregular waves, Adv. Energy Mater. 15 (2024) 2404891.
[27] C. Chen, D. Guo, L. Tuo, Y. Wen, J. Li, H. Qu, H. Wen, L. Wan, G. Liu, H. Guo, One meter triboelectric nanogenerator for efficient harvesting of meter-scale wave energy, Adv. Funct. Mater. 34 (2024) 2406775.
[28] Y. Wang, H. Du, H. Yang, Z. Xi, C. Zhao, Z. Qian, X. Chuai, X. Peng, H. Yu, Y. Zhang, X. Li, G. Hu, H. Wang, M. Xu, A rolling-mode triboelectric nanogenerator with multi-tunnel grating electrodes and opposite-charge-enhancement for wave energy harvesting, Nat. Commun. 15 (2024) 6834.
[29] B. Zhao, Z. Li, X. Liao, L. Qiao, Y. Li, S. Dong, Z. Zhang, B. Zhang, A heaving point absorber-based ocean wave energy convertor hybridizing a multilayered soft-brush cylindrical triboelectric generator and an electromagnetic generator, Nano Energy 89 (2021) 106381.
[30] P. Chen, J. An, R. Cheng, S. Shu, A. Berbille, T. Jiang, Z.L. Wang, Rationally segmented triboelectric nanogenerator with a constant direct-current output and low crest factor, Energy Environ. Sci. 14 (2021) 4523–4532.
[31] H. Li, S. Lv, B. Zhang, B. Liu, J. Yang, H. Guo, Y. Xie, Z. Lin, High power and low crest factor of direct-current triboelectric nanogenerator for self-powered optical computing system, Energy Environ. Sci. 16 (2023) 4641–4649.
[32] X. Li, X. Yin, Z. Zhao, L. Zhou, D. Liu, C. Zhang, C. Zhang, W. Zhang, S. Li, J. Wang, Z.L. Wang, Long-lifetime triboelectric nanogenerator operated in conjunction modes and low crest factor, Adv. Energy Mater. 10 (2020) 1903024.
[33] H. Ryu, J.H. Lee, U. Khan, S.S. Kwak, R. Hinchet, S.M. Kim, Sustainable direct current powering a triboelectric nanogenerator via a novel asymmetrical design, Energy Environ. Sci. 11 (2018) 2057–2063.
[34] R.D.I.G. Dharmasena, H.M. Cronin, R.A. Dorey, S.R.P. Silva, Direct current contact-mode triboelectric nanogenerators via systematic phase shifting, Nano Energy 75 (2020) 104887.
[35] Z. Wu, S. Wang, Z. Cao, R. Ding, X. Ye, Rotary disk multi-phase freestanding-electret generator with enhanced power and low ripple output, Nano Energy 83 (2021) 105787.
[36] J. Wang, Y. Li, Z. Xie, Y. Xu, J. Zhou, T. Cheng, H. Zhao, Z.L. Wang, Cylindrical direct-current triboelectric nanogenerator with constant output current, Adv. Energy Mater. 10 (2020) 1904227.